# Crystal growth, magnetic and magnetocaloric properties of $J_{\text{eff}} = 1/2$ quantum antiferromagnet $CeCl_3$

Nashra Pistawala,[1] Luminita Harnagea,[2] Suman Karmakar,[3] Rajeev Rawat,[3] and Surjeet Singh[1,*]

[1]*Department of Physics, Indian Institute of Science Education and Research, Pune 411008, India*

[2]*I-HUB Quantum Technology Foundation, Indian Institute of Science Education and Research, Pune 411008, India*

[3]*UGC-DAE Consortium for Scientific Research, University Campus, Khandwa Road, Indore 452 001, India*

(Received 18 April 2023; revised 27 April 2024; accepted 20 May 2024; published 1 July 2024)

We report growth of high-quality single crystals of $CeCl_3$ using a modified Bridgman-Stockbarger method in an infrared image furnace. The grown crystals are characterized using single-crystal(powder) x-ray diffraction, Laue x-ray diffraction, Raman spectroscopy, magnetization, and heat-capacity probes. $CeCl_3$ crystallizes in a hexagonal structure ($P6_3/m$) with a weak trigonal distortion ($P\bar{3}$). The Raman spectrum at 300 K shows five clearly resolvable phonon modes at 106.8, 181.2, 189, 213, and 219.7 $cm^{-1}$. The magnetic susceptibility along $H \parallel c$ ($\chi^{\parallel}$) and $H \perp c$ ($\chi^{\perp}$) axis is measured as a function of temperature and magnetic field. $\chi^{\perp}$ exhibits a broad peak centered around 50 K; $\chi^{\parallel}$, in comparison, shows a monotonic Curie-like increase upon cooling and is about two orders of magnitude larger in size. This anisotropic behavior with qualitatively different temperature dependences shown by $\chi^{\parallel}$ and $\chi^{\perp}$ is explained using the crystal field theory. The crystal field in $CeCl_3$ splits the $J = 5/2$ manifold of $Ce^{3+}$ into three Kramers doublets with $|5/2, \pm 5/2\rangle$ as the ground state, and $|5/2, \pm 1/2\rangle$ at energy $E_1 = 61$ K, and $|5/2, \pm 3/2\rangle$ at $E_2 = 218$ K as the first and second excited states, respectively. Accordingly, $M(H)$ at 2 K along $H \perp c$ is small and shows a linear variation, whereas $M$(H) along $H \parallel c$ saturates readily (*easy* axis) to the expected value. In the specific heat, no magnetic ordering could be seen down to 2 K. However, in nonzero fields the low-temperature specific heat changes dramatically, showcasing a peak at 2.5 K under a moderate field of 30 kOe. The weak Ce-Ce exchange, large Ce moment in the crystal-field ground state, and huge anisotropy are all ingredients for realizing a high magnetocaloric effect. Indeed, measurements at low temperatures reveal a maximum entropy change of $-\Delta S_{4f} \approx 23 \pm 1$ J Kg$^{-1}$ K$^{-1}$ near 2.5 K in the field ranging from 50 to 60 kOe. These values are comparable to some of the best known Gd-based magnetocaloric materials, signifying the potential of $CeCl_3$ as a magnetic coolant.

DOI: 10.1103/PhysRevMaterials.8.076201

## I. INTRODUCTION

Quantum antiferromagnets have garnered enormous attention in recent years. They exhibit exotic phases at low temperatures including quantum spin liquids (QSLs) with fractional excitations and long-range entanglement [1]. The triangular and kagome lattice antiferromagnets are ideal platforms to realize the QSL phase. In 2006, Alexie Kitaev proposed an exactly solvable model comprising anisotropic spin-1/2 particles on a honeycomb lattice whose ground state is also a QSL with Majorana fermions as the quasi-particle excitations [2]. However, unlike geometrical frustration, where the geometry of the underlying lattice gives rise to competing interactions, in the Kitaev model, it is the bond-dependent Ising-like interactions that result in strong spin frustration [3]. The iridates (e.g., $Na_2IrO_3$) and the ruthenates (e.g., $\alpha-RuCl_3$) have been extensively studied to realize the Kitaev model [4]. The search for a half-quantization plateau in the thermal Hall effect in $\alpha$-$RuCl_3$, which would confirm the existence of Majoranas, is currently a topic of intense research in quantum condensed matter [5,6]. Recently, $YbCl_3$, has also attracted attention as a quantum antiferromagnet with a honeycomb lattice of the $Yb^{3+}$ ions in their Kramers doublet ground state ($J_{\text{eff}} = 1/2$) [7–9]. $YbCl_3$ belongs to the rare-earth trichloride family with the general formula $RCl_3$ (R = rare − earth element). While the heavier rare-earth members ($R$ = Tb to Lu) of this series crystallize with a monoclinic structure analogous to $\alpha-RuCl_3$, the lighter members ($R$ = La to Gd) crystallize with a hexagonal structure where the $R^{3+}$ ions arrange on triangular plaquettes, stacked to form $R^{3+}$ chains running parallel to the $c$ axis [10–12]. Here, we focus on the hexagonal member $CeCl_3$ of this series. $CeCl_3$ is an antiferromagnetic insulator with an electronic band gap of 4.2 eV [13]. Both $Yb^{3+}$ and $Ce^{3+}$ are Kramers ions, but while $Yb^{3+}$ is just one short of the completely filled $f$ shell, $Ce^{3+}$ has only one electron in the $f$ shell, making it a potential quantum magnet analogous to $YbCl_3$, albeit with a different lattice structure. The previous reports on $CeCl_3$ concentrated only on the low-temperature behavior ranging from 0.1 K to 4.2 K and magnetic fields up to 12 kOe [14]. The Cl and Br nuclear quadrupole resonance (NQR) on some rare-earth trichlorides and tribromides, including $CeCl_3$, was reported previously over the same temperature range [15]. According to these reports, in $CeCl_3$, the $Ce^{3+}$ ions are in an effective spin 1/2 state, and they

*Contact author: surjeet.singh@iiserpune.ac.in

 

undergo long-range antiferromagnetic ordering below 1 K. The ordering temperature however shows a strong sample dependence, which has been attributed to the presence of impurities in the grown crystals [14,16]. Recently, interest in $CeCl_3$ has been reinvigorated with some theoretical studies predicting the emergence of optically driven chiral phonon modes, generating giant effective magnetic fields ($\sim 10^2$ T) acting on the paramagnetic $4f$ spins [17,18]. Motivated by these new theoretical studies and the fact that the magnetic and thermodynamic properties of $CeCl_3$ are largely unexplored above 4.2 K where the crystal electric field split levels of Ce are expected to dominate the physical properties, we decided to grow and investigate $CeCl_3$.

In this study, we report the crystal growth, structural, magnetic, and thermodynamic characterizations of high-quality single crystals of $CeCl_3$. We show that the magnetic susceptibility of $CeCl_3$ shows a large anisotropy that originates from the crystal electric-field splitting of the lowest $J$ multiplet of $Ce^{3+}$. The susceptibility along the two orientations is fitted using the crystal electric-field analysis. The low-temperature specific heat is found to change substantially in the presence of an applied magnetic field, showcasing a peak at 2.5 K under a field of 30 kOe. Due to the large magnetic anisotropy, a sizable ground-state magnetic moment, and significant variation in the specific heat under applied magnetic fields, the magnetocaloric assessment revealed a high maximum-magnetic entropy change of $-\Delta S_{4f} = 23 \pm 1$ J Kg$^{-1}$ K$^{-1}$ near 2 K for $\Delta H = 6$ T.

## II. EXPERIMENTAL METHODS

Single crystals of $CeCl_3$ are grown from a stoichiometric melt using the two different methods: the static Bridgman method and the traditional Bridgman-Stockbarger method in an image furnace. The details of the crystal-growth methods and experiments are given in Sec. III A. The single-crystal specimens for various experiments were cut inside an Ar-filled glovebox to prevent decomposition upon exposure to the atmospheric air. For this purpose, the crystals were embedded in a thin layer of mounting wax (used for sample cutting or polishing) before being taken out of the glove-box. At the end of the experiment, the wax layer was dissolved inside the glovebox using dichloromethane ($CH_2Cl_2$), which is both water repellent and anhydrous. Single-crystal x-ray diffraction was carried out using a Bruker Smart Apex Duo diffractometer at 100 K using Mo K$\alpha$ radiation ($\lambda = 0.71073$ Å). The total exposure time was 2.01 h. The frames were integrated using the Bruker SAINT software package employing a narrow frame algorithm. Data were corrected for absorption effects using the multiscan method (SADABS). The structure has been solved and refined using the Bruker SHELXTL software package. The grown crystals were oriented using a Laue camera (Photonic Science, UK) in backscattering geometry using tungsten as a source material ($\lambda = 0.35 - 2.5$ Å, accelerating voltage 30 kV, and tube current 0.3 mA). The Laue pattern was analyzed using ORIENT EXPRESS 3.4 (V 3.3) software package. Raman spectra were collected at room temperature in backscattering configuration using a Horiba Jobin-Yvon LabRAM HR spectrometer equipped with liquid nitrogen cooled charge-coupled detector and a laser of 532 nm as a source of excitation. The excitation was maintained at 25% of the maximum power, and the accumulation time for each spectrum was 30 s with 25 iterations each time to get better resolution and intensity of the Raman modes. The $CeCl_3$ crystal was coated with a thin layer of Apiezon N grease to prevent degradation due to its extremely hygroscopic nature. The Raman signal from the Apiezon N was measured separately and subtracted from the total signal to eliminate the background. The Specific-heat measurements were done using the relaxation method in a Physical Property Measurement System (PPMS), Quantum Design, USA. A small piece of crystal was cut into a 2 mm × 2 mm piece, weighing around 10 mg, mounted on the heat-capacity sample holder using a low-temperature Apiezon N grease. The addenda (heat capacity of the sample holder and Apiezon N grease) was measured before loading the sample. Sample degradation from moisture is minimized by handling, weighing, and cutting of the specimens inside the glovebox. The magnetic susceptibility was measured at the UGC-DAE CSR, Indore center, Indore, using a vibrating-sample magnetometer probe option in a PPMS, Quantum Design, USA.

## III. RESULTS AND DISCUSSION

### A. Specific difficulties in the crystal growth of $CeCl_3$

The anhydrous rare-earth trichlorides ($RCl_3$) in general and $CeCl_3$ in particular are highly sensitive to the presence of moisture in air, reacting readily to form $RCl_3.xH_2O$ ($x \approx 6$), especially during a humid day when this reaction happens over a timescale of a few minutes. It is therefore difficult to grow large single crystals of rare-earth trichlorides from a melt as the adsorbed moisture, when not carefully removed, reacts with $RCl_3$ to form various oxychlorides (e.g., $ROCl$) and oxides, which makes the melt hazy. The grown crystal in such cases also has a hazy appearance with a large number of cracks. It is, therefore, necessary to remove the absorbed moisture. In Ref. [19], this is done using ammonium chloride or the halides of carbon or sulfur as the cleaning agents. Such cleansing methods, however, have their own drawback as they tend to introduce undesirable impurities (rare-earth carbides or sulfides in the precursor materials) [19].

To avoid this, in a previous study, the crystals of rare-earth trichlorides were grown using the chemical vapor transport method employing $AlCl_3$ as the transporting agent [20]. In this reaction, the rare-earth ($R$) oxides are first reacted with $AlCl_3$ to form corresponding anhydrous rare-earth trichlorides. These are then further reacted with an excess $AlCl_3$ through a reversible reaction to form gaseous complexes, including $RAl_3Cl_{12}$ and $RAl_4Cl_{15}$. These gaseous complexes, having a significantly high vapor pressure, are transported to the colder end of the tube, where millimeter-sized transparent crystals of $RCl_3$ can be extracted. This method is, however, complex and the resulting crystals are small and not of very high quality. Mroczkowski *et al.* reported crystal growth of $EuCl_3$ using the vertical Bridgman method in the presence of $Cl_2$ gas under high pressure [21]. They purified the hydrated precursor by placing it in a stream of HCl gas before subjecting it to crystal growth. A similar method was later cited for the crystal growth of $CeCl_3$ in Ref. [14]. However, the

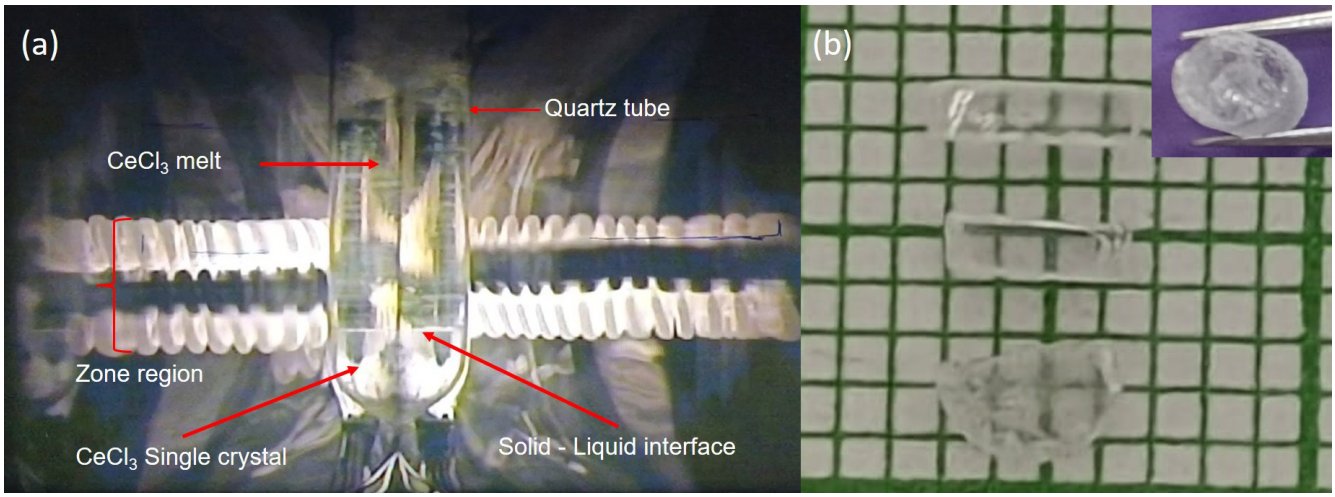


FIG. 1. (a) Crystal growth of $CeCl_3$ using a four-mirror image furnace equipped with 1 kW halogen lamps. The lower part below the solid-liquid interface is the $CeCl_3$ crystal being grown. (b) Images of the crystal pieces obtained after cutting the crystal boule shown in the inset.

use of corrosive HCl gas raises safety, health, and environmental concerns. These complex approaches described in the previous studies may not be necessary presently due to the availability of high-quality precursor materials. We, therefore, used a relatively simpler approach to obtain high-quality single crystals of $CeCl_3$. Our method involves a simple purifying step followed by crystal growth from the stoichiometric melt described in the following paragraph.

In our method, the anhydrous $CeCl_3$ powder (Alfa Aesar 99.9%) was stored and handled in an argon filled glove box where $O_2$ and moisture levels are maintained below 0.1 ppm at all times. In the first step, the as-purchased $CeCl_3$ powder was heat-treated under a dynamic vacuum. For this, the quartz ampoule used was preheated overnight at 1000 °C to remove any adsorbed moisture. This ampoule was then transferred into the glove-box at 200 °C, with its open end temporarily sealed using a bottle-cork. Inside the glove-box, the ampoule was loaded with the $CeCl_3$ powder, taken out of the glove-box and connected to a turbomolecular pump. The $CeCl_3$ powder is then gradually heated in a furnace up to a temperature of 230 °C. After heating at this temperature for 24 h under dynamic vacuum, the ampoule was allowed to cool down to room temperature before flame-sealing under dynamic vacuum ($\sim 10^{-5}$ mbar). Up to here, the procedure is common for both the methods outlined below.

### *1. Static Bridgman*

In static Bridgman method, the sealed ampoule was placed in a vertical tubular furnace under a temperature gradient. The furnace was heated to 870 °C, which is higher than the melting point of anhydrous $CeCl_3$ (817 °C), at a rate of 50 °C/h and allowed to dwell at this temperature for 12 h. After this, the furnace was slowly cooled to 750 °C at a rate of 0.3 °C/h, and finally cooled down to room temperature at a rate of 50 °C/h. Shiny transparent crystals measuring up to a few millimeters in size were extracted from the ampoule.

### *2. Bridgman-Stockbarger*

In this case, the quartz ampoule used was around 4–5 mm in inner diameter and 8 mm in outer diameter. In the first step of this method, the $CeCl_3$ loaded ampoule was placed in a muffle furnace and heated up to 850 °C to obtain a premelted, highly dense ingot, about 15–20 mm long, which was subsequently subjected to crystal growth in an infrared image furnace. For this purpose, the quartz ampule containing the premelted ingot was loaded into a four-mirror image furnace by suspending it to the upper shaft of the furnace [see Fig. 1(a)]. The shaft was positioned such that the lower end of the ampoule reaches the center of the furnace (the common foci of the four ellipsoidal reflectors), which is the region where the molten-zone forms during the normal floating zone experiment [22]. The lamp power was then gradually raised until $CeCl_3$ melted. Once a homogenous melt is achieved, the ampoule is made to travel vertically downwards, out of the hot-zone, and into a region with a steep vertical temperature gradient. The lamps used were 1 KW each and are estimated to give a vertical temperature gradient, outside the molten zone, of several hundred °C/cm. In order to optimize the growth parameters for obtaining crack-free, high-quality crystals, several growth experiments were conducted at various traveling speeds, varying from 1 mm $h^{-1}$ to 0.2 mm $h^{-1}$. At 1 mm $h^{-1}$, the crystal boule developed numerous cracks yielding very small, irregularly shaped, crystal pieces. At slower growth speeds the results improved, but even at the slowest growth speed of 0.2 mm $h^{-1}$ the cracks could not be avoided completely. In this case, however, the cracks were fewer, and hence large crystal pieces, several millimeter long by several millimeters across, could be obtained. The crystals were cut inside the glovebox using a low-speed saw. While cutting, small rectangular crystal pieces cleaved off the crystal boule. These crystal pieces are found to be fully transparent with atomically flat facets as shown in Fig. 1(b). The flat surfaces of the semicircular piece in Fig. 1(b) were dry polished using a silicon-carbide paper of grit size 1200. The slight haziness seen is due to imperfect surface polishing and not because the crystal piece is hazy inside.

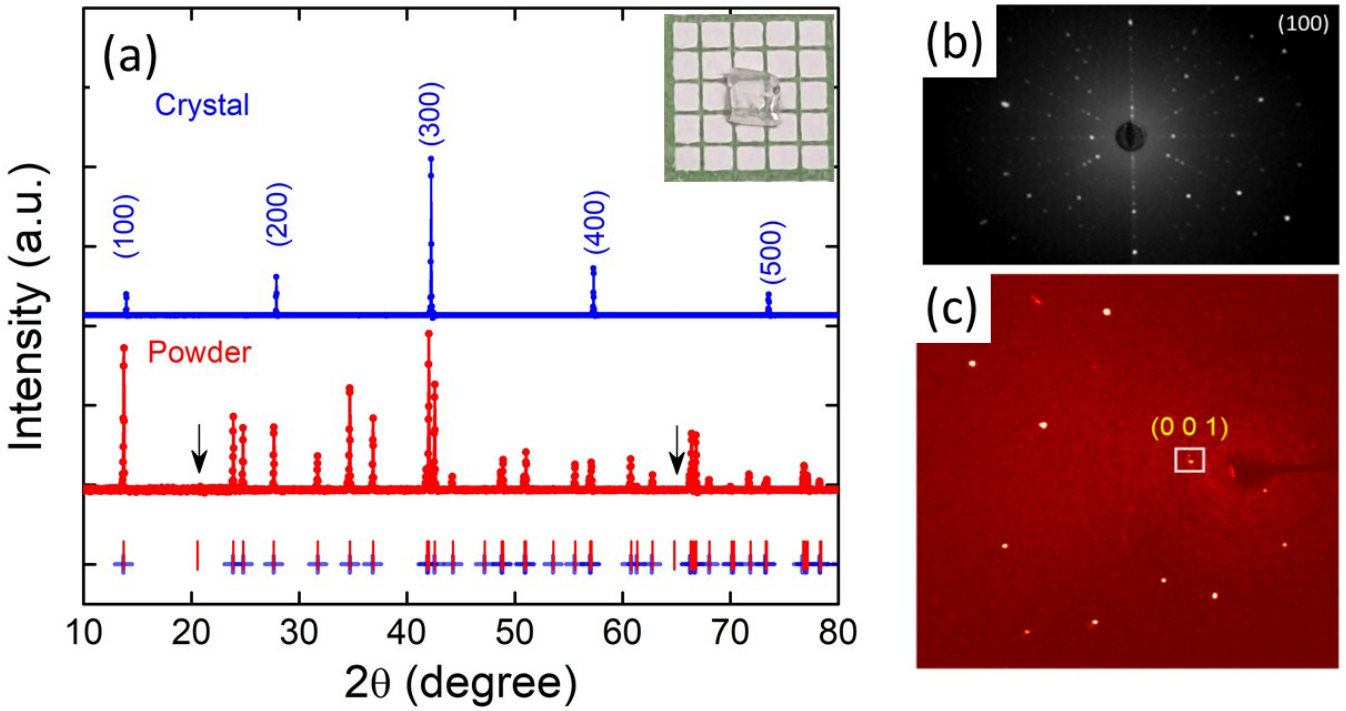


FIG. 2. (a) The x-ray-diffraction pattern of a single-crystal specimen of $CeCl_3$ in the Bragg-Brentano geometry (blue); the powder x-ray-diffraction pattern of $CeCl_3$ obtained by crushing a small crystal piece (red); the calculated Bragg positions for hexagonal (+) and trigonal (|) symmetries. The arrows indicate the positions of (0 0 1) and (0 0 3) peaks in the trigonal symmetry. (b) The x-ray Laue diffraction pattern, and (c) a raw frame during the single-crystal x-ray-diffraction data, where the (0 0 1) spot is marked. Inset in (a) shows a representative crystal specimen used in the x-ray-diffraction experiments.

Between the two growth methods, the crystals obtained using the image furnace are of higher quality. They are fully transparent and hence one can say are essentially defect-free. The presence of defects or impurities (typically oxychlorides and oxides mentioned above) in the crystal leads to hazy or milky appearance. Analysis of impurities in the grown crystals is summarized in Fig. S1 (see Supplemental Material) [23]. Figure 2(a) shows the x-ray diffraction pattern recorded in the Bragg-Brentano geometry on a flat crystal specimen, such as the one shown in the inset of Fig. 2(a). The only diffraction peaks seen are the ones corresponding to the crystallographic *bc*-plane. This shows that the specimen used for this experiment is an oriented single crystal of high-quality. The orientation of the surface was further confirmed using x-ray Laue diffraction [see Fig. 2(b)], where sharp Laue spots were observed, which confirms that the grown crystals are of high quality.

### B. Single-crystal x-ray diffraction

A small crystal specimen was selected for single-crystal x-ray diffraction (SCXRD). A detailed examination of the collected diffraction data was carried out to establish the crystal structure of $CeCl_3$. The data were collected at $T = 100$ K. The SCXRD data refinement was done using two different structural models, namely, hexagonal and trigonal. As far as diffraction is concerned, the essential difference between these structures lies in the presence or absence of (0 0 $l$) reflections, where $l = (2n + 1)$. In the trigonal symmetry, these reflections are allowed, whereas in the hexagonal symmetry, they are forbidden. In the raw frames, weak (0 0 $l$) reflections could be identified, as shown in Fig. 2(c) (see also Fig. S2 in the Supplemental Material for more raw frames) [23]. These reflections are better depicted in Fig. S3, where the reconstructed $h0l$ reciprocal-space planes and three-dimensional plots of the (0 0 $l$) reflections are presented. The presence of weak (0 0 1) and (0 0 3) reflections can be seen unambiguously. This is further corroborated by the structural refinement data. In the trigonal case, all the diffraction spots can be successfully indexed, with no systematic absences observed. Conversely, in the hexagonal model, the (0 0 $l$) reflections remain unindexed. In both cases, we used the observability criterion $I > 3\sigma(I)$, where $\sigma(I)$ is the standard deviation in the intensity distribution. The intensity ($I$) and the corresponding $\sigma(I)$ values for the unindexed reflections under the hexagonal space group are listed in Table S2 in the Supplemental Material [23]. A comparison of structural refinement parameters for the two models is outlined in Table I below. The goodness of fit and $R_{\text{int}}$ values favor the trigonal structure, but the difference in their values is not overwhelming. This is also reflected in the structural parameters obtained in the two cases. For example, in the trigonal model, the space group is $P\bar{3}$ (# 147) and the corresponding Wyckoff sites are: Ce($2d$) with fractional coordinate ($\frac{2}{3}$, $\frac{1}{3}$, $z_{\text{Ce}}$) and Cl($6g$) with fractional coordinates ($x_{\text{Cl}}$, $y_{\text{Cl}}$, $z_{\text{Cl}}$). The best-fit values obtained for these coordinates are $z_{\text{Ce}} = 0.250\,04(8)$ and $x_{Cl} = 0.913\,50(14)$, $y_{\text{Cl}} = 0.612\,49(15)$, $z_{\text{Cl}} = 0.7500(3)$. On the other hand, in the hexagonal case, the space group is $P6_3/m$ (176), and the Wyckoff sites are: Ce($2c$) with fixed

TABLE I. Summary of refinement parameters for two different models.

| Model | | A | B |
|---|---|---|---|
| Crystal system | | Trigonal | Hexagonal |
| Space group | | $P\bar{3}$ (147) | $P6_3/m$ (176) |
| Goodness of fit | | 1.292 | 1.372 |
| $R_{int}$ (%) | | 4.45 | 4.85 |
| Final $R$ indices (%) | $R_1$ | 2.50 | 2.47 |
| | $wR_2$ | 6.54 | 6.04 |
| Number of refined parameters | | 14 | 10 |

fractional coordinates $(\frac{2}{3}, \frac{1}{3}, \frac{3}{4})$ and Cl($6h$) with fractional coordinates $(x_{Cl}, y_{Cl}, \frac{1}{4})$, where $x_{Cl} =$ 0.913 48(15), $y_{Cl} =$ 0.612 56(16). The coordinates $z_{Ce}$ and $z_{Cl}$ in the trigonal symmetry relate to the hexagonal case by $1 - z$. On the other hand, the $x$ and $y$ coordinates of Cl in the two cases differ minutely. Besides this difference, and the minute differences in the bond lengths and bond angles, the two structures nearly overlap. To conclude, though the crystal structure of $CeCl_3$ is trigonal in the true sense, in practical terms, it deviates from the hexagonal symmetry only marginally. The summary of crystallographic data using the trigonal model is shown in Table II. The data collection and structure refinement parameters are summarized in Table S3 in the Supplemental Material [23] and the atomic coordinates of Ce and Cl along with their isotropic displacement parameters are listed in Table S4 in the Supplemental Material [23].

The calculated powder x-ray-diffraction profile shows zero intensity for the (0 0 1) and (0 0 3) lines. The nonzero intensity of these peaks requires the $z$ coordinate of Ce in the trigonal structure to differ sufficiently from the value in the hexagonal case, or for the Cl atoms at 6$g$ (trigonal) or 6$h$ (hexagonal) to have substantially different coordinates in the two structures. Since the differences in the variable coordinates in the two structures are minor, it will be practically impossible to detect the (0 0 1) or (0 0 3) lines in the powder pattern. The measured powder x-ray-diffraction pattern shown in Fig. 2(a) confirms

TABLE II. Summary of the crystallographic data in the trigonal model.

| Chemical formula | $CeCl_3$ | |
|---|---|---|
| Formula weight | 246.47 g/mol | |
| Temperature | 100 K | |
| Wavelength | 0.71073 Å | |
| Crystal system | Trigonal | |
| Space group | $P$ -3 | |
| Unit-cell dimensions | $a = 7.4242(15)$ Å | $\alpha = 90°$ |
| | $b = 7.4242(15)$ Å | $\beta = 90°$ |
| | $c = 4.3189(13)$ Å | $\gamma = 120°$ |
| Volume | 206.16(10) Å$^3$ | |
| $Z$ | 2 | |
| Density (calculated) | 3.970 g/cm$^3$ | |
| Absorption coefficient | 12.742 mm$^{-1}$ | |
| $F(000)$[a] | 218 | |

[a]$F(000)$ is a structure factor calculated at $h = k = l = 0$ and indicates the effective number of electrons in the unit cell.

this assertion, as the superstructure lines could not be detected beyond uncertainty. The (0 0 1) line may possibly be picked in a longer run, but keeping the sample undecomposed over a longer duration, even in an airtight sample holder, is a challenge. Using synchrotron-based experiments, one can try to overcome this challenge. To summarize the deviation from the ideal hexagonal structure is so minor that for all practical purposes one can consider the structure of $CeCl_3$ to be hexagonal, in agreement with the previous symmetry assessment based on the powder x-ray diffraction data [10–12].

In both the structures, each $Ce^{3+}$ ion is ninefold coordinated by $Cl^-$ ions, as shown in Fig. 3(c). Of these, three $Cl^-$ are coplanar with the central $Ce^{3+}$ ion. These are labeled 1, 2, and 3 in Fig. 3(c). The other six $Cl^-$ ions are located in planes parallel to this plane, located above and below the central $Ce^{3+}$ ion. These are labeled as 4, 5, and 6 (above), and 7, 8, and 9 (below) in Fig. 3(c). In the $ac$ plane, shown in Fig. 3(a), the $Ce^{3+}$ ions form a zigzag chain running parallel to the $c$ axis. The bond distances for the trigonal case are also shown in Fig. 3. The Ce ions marked with a yellow border are located at a distance of 4.319 Å from the central Ce ion (blue) along the $c$ axis. This is the nearest-neighbor (*nn*) Ce-Ce distance. The three second-nearest neighbors (*nnn*) are at a distance of 4.799 Å. They are shown with a pink border for easy identification. The third nearest-neighbor (*nnnn*) distance is 7.424 Å. The third neighbors are shown with a red border, as in Fig. 3(b). The polyhedra around the $Ce^{3+}$ ions are edge shared, forming a hexagonal ring in the $ab$ plane as shown in Fig. 3(b). The magnetic exchange path between any two nearest-neighbor Ce ions is via three Ce–Cl–Ce pathways along the $c$ axis, where the Ce–Cl–Ce bond angle is 95.4°, as shown in Fig. 3(d). The *nnn* interaction is mediated via two Ce–Cl–Ce pathways with bond angle Ce–Cl–Ce of 110.1°, as shown in Fig. 3(e). Since these bond angles do not differ from each other greatly, the strength of *nn* and *nnn* exchange interaction is expected to be comparable.

### C. Raman spectrum

Figure 4 shows the Raman spectrum of a high-quality single crystal of $CeCl_3$. The observed spectrum is satisfactorily fitted using *five* Lorentzian line shapes. For simplicity, the modes are labeled from $R_1$ to $R_5$ and their positions are 106.8, 181.2, 189, 213, and 219.7 cm$^{-1}$. In an older study, $CeCl_3$ is reported to show six Raman modes at $E_{2g}$ (106 cm$^{-1}$), $A_g$ (176 cm$^{-1}$), $E_{2g}$ (180 cm$^{-1}$), $E_{1g}$ (193 cm$^{-1}$), $A_g$ (216 cm$^{-1}$), and $E_{2g}$ (218 cm$^{-1}$) [25]. The comparison with our data suggests the presence of an extra peak at 176 cm$^{-1}$ in the spectra reported in Ref. [25]. Incidentally, in the isostructural $LaCl_3$ only five Raman modes are reported at 108, 179, 186, 210, and 217 cm$^{-1}$ [26]. The extra mode in $CeCl_3$, as seen in Ref. [25], can be due to the presence of local defects or impurities. Although the polarization dependence of the mode $R_2$ was previously reported [25], a more careful polarization-dependent study of the entire spectrum is lacking. Also, a temperature- and magnetic-field dependent study on high-quality crystals is needed to understand the evolution of Raman modes with temperature and magnetic field. Previously, it was reported that the degenerate $E_{1g}$ and $E_{2g}$ Raman

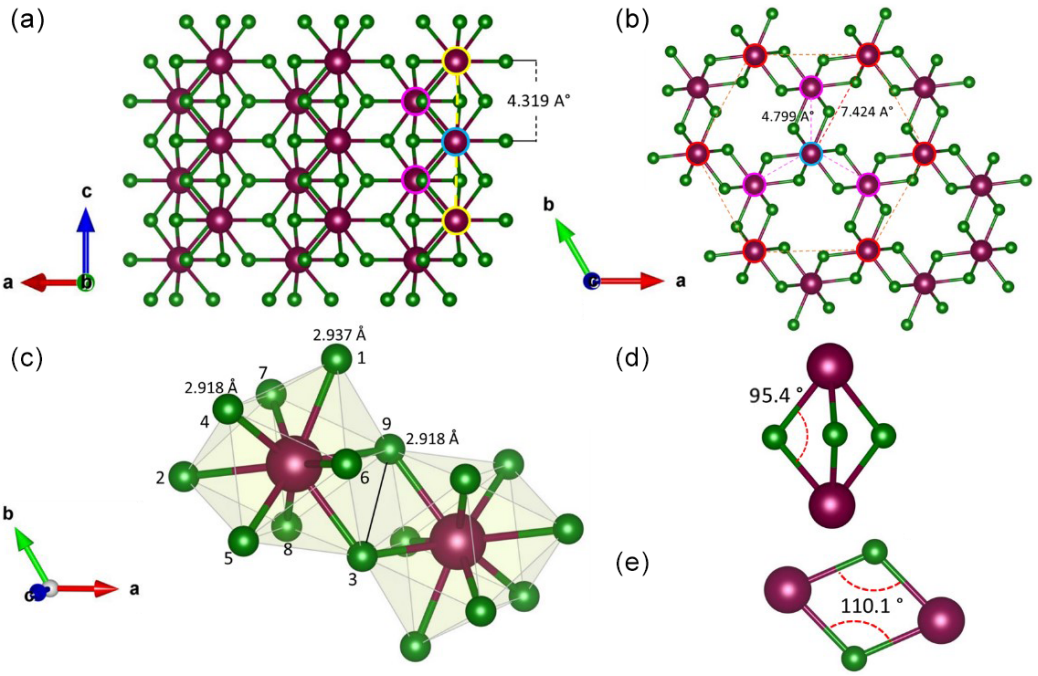


FIG. 3. Crystal structure of $CeCl_3$ obtained using VESTA [24]. (a) As viewed along the *b* axis (*ac* plane). (b) As viewed along the *c* axis (*ab* plane). The large (brown) and smaller (green) balls represent Ce and Cl ions, respectively. The nearest neighbor (*nn*), next *nn*, and next to next *nn* Ce ions are in yellow magenta and red borders, respectively; (c) Ninefold coordination of $Ce^{3+}$ ions where $Cl^-$ ions numbered 1, 2, and 3 are coplanar with the central $Ce^{3+}$ ion. The $Cl^-$ ions numbered 4–6 lie in a plane above and 7–9 in a plane below the plane formed by 1–3. These planes are perpendicular to the *c* axis; (d) Ce-Cl-Ce nearest-neighbor exchange pathways via 95.4° angle; (e) Ce-Cl-Ce next nearest neighbor exchange pathways via 110.1° angle.

modes split under magnetic field into left- and right-handed circular polarization, leading to a chiral behavior [27]. With the availability of high-quality single crystals of $CeCl_3$, such experiments involving temperature and field dependence will be carried out in future.

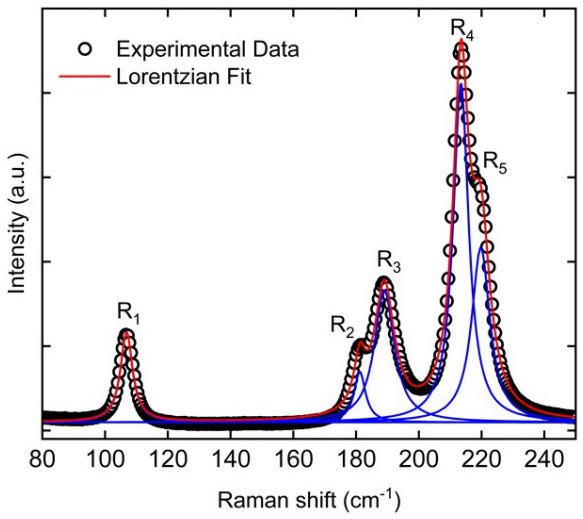


FIG. 4. The Raman spectra of $CeCl_3$. The five Raman modes are labeled $R_1$, $R_2$, ..., $R_5$. The blue curves are individual Lorentzian fit to each mode. The red line through the data points is the total fitted spectrum obtained by adding the individual Lorentzians. The raw data up to 550 $cm^{-1}$ are shown in Fig. S4 in the Supplemental Material [23].

### D. Magnetic susceptibility

#### *1. Curie-Weiss analysis*

The magnetic susceptibility of $CeCl_3$ is measured under a magnetic field of 1 kOe for two different orientations, namely $H \parallel c$ and $H \perp c$ axis. Additionally, measurements are also done on a powder specimen of $CeCl_3$, obtained by crushing a small crystal piece. The magnetic susceptibility plots are shown in Fig. 5. The susceptibility measurements are performed in both zero-field cooled (ZFC) and field-cooled (FC)

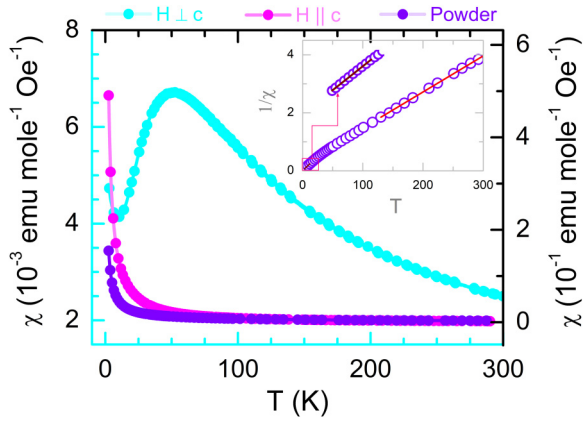


FIG. 5. The magnetic susceptibility $\chi$ is plotted as a function of temperature for H $\parallel$ *c*, H$\perp$*c*, and powder specimens of $CeCl_3$. Inset shows the inverse magnetic susceptibility as a function of temperature for the powder sample. The solid lines in the inset represent Curie-Weiss fit (see text for details). In the main panel, the lines are used as a guide to the eye.

TABLE III. The fitting parameter in the Curie-Weiss fit of the susceptibility data for single crystal and powder sample.

| | Fitting range (K) | $\chi_0$ (emu mole$^{-1}$ Oe$^{-1}$) | C (emu mol$^{-1}$ Oe$^{-1}$ K) | $\mu_{\text{eff}}$ ($\mu_B$) | $\Theta_{\text{cw}}$ (K) |
|---|---|---|---|---|---|
| $H \parallel c$ | 150–300 | $-5.1 \times 10^{-4}$ | 0.81 | 2.54 | 18.7 |
| | 3–10 | $-2.3 \times 10^{-3}$ | 1.47 | 3.42 | 0.017 |
| $H \perp c$ | 200–300 | $2.7 \times 10^{-4}$ | 0.75 | 2.46 | −32.7 |
| | 3–7 | $3.8 \times 10^{-3}$ | 0.003 | 0.15 | −0.39 |
| Powder | 130–300 | $8.8 \times 10^{-4}$ | 0.81 | 2.54 | −18.2 |
| | 3–10 | $1.8 \times 10^{-3}$ | 0.47 | 1.95 | −0.12 |

modes. The two runs exactly overlap and hence only ZFC run is shown in Fig. 5. Upon cooling, $\chi^{\perp}(T)$ [i.e., $\chi(T)$ for $H \perp c$] exhibits a broad peak at 50 K, followed by a sharp increase below 9 K, as shown in Fig. 5. In contrast, $\chi^{\parallel}$ is almost two orders higher in magnitude and is characterized by a monotonically increasing behavior with decreasing temperature. The broad peak in $\chi^{\perp}(T)$ is due to the crystalline electric-field (CEF) splitting of the $J = 5/2$ ground state of $Ce^{3+}$. The CEF splitting scheme for $Ce^{3+}$ is discussed in the next section. The Curie-Weiss analysis was performed in the low- and high-temperature ranges for both orientations and the powder sample. Due to the presence of a small curvature in $\chi^{-1}$, we used the modified Curie-Weiss expression, $\chi = \chi_0 + C/(T - \Theta_{cw})$, where $\chi_0$, $C$, and $\Theta_{cw}$ represent the temperature independent van Vleck contribution, Curie constant, and Curie-Weiss temperature, respectively. The symbols $\chi_0^{||}$, $\chi_0^{\perp}$; $C^{||}$, $C^{\perp}$; and $\Theta_{cw}^{\parallel}$, $\Theta_{cw}^{\perp}$ are used to replace $\chi_0$, $C$, and $\Theta_{cw}$ in the Curie-Weiss expression for $H \parallel c$ and $H \perp c$ orientations, respectively. The value of $\mu_{\text{eff}}$ can be obtained from the Curie constant using the expression $\mu_{\text{eff}} = \sqrt{8C}$. The results are summarized in Table III. The fitting for the powder specimen is shown in the inset of Fig. 5, as a representative case.

The analysis of H $\parallel c$ data yields the following values of the fitting parameters: $\chi_0^{\parallel} \sim -5.1 \times 10^{-4}$ emu mol$^{-1}$ Oe$^{-1}$, and $C^{||} = 0.81$ emu mol$^{-1}$ Oe$^{-1}$ K giving $\mu^{||}{}_{\text{eff}} = 2.53(1)$ $\mu_B$/Ce. This value of $\mu_{\text{eff}}$ matches closely with the theoretical value of 2.54 $\mu_B$/Ce calculated using $J = 5/2$ and $g_J = \frac{6}{7}$, where $J$ is the total angular momentum and $g_J$ is the Landé $g$ factor. The value of $\Theta_{cw}^{\parallel} = 18.7$ K is positive, indicating that the Ce-Ce interaction along the $c$ axis is ferromagnetic. The large value of $\Theta_{cw}^{\parallel}$ compared to the long-range antiferromagnetic ordering temperature ($T_{\text{N}} \sim 0.1$ K [14]) is simply an artifact arising due to the large crystal-field splitting. The low-temperature fitting is performed in the range 3 K $< T <$ 10 K, yielding $C^{||} = 1.47$ emu mol$^{-1}$ Oe$^{-1}$ K or an effective magnetic moment of 3.42 $\mu_B$/Ce. As we show below, at low temperatures, only the lowest Kramers doublet $|5/2, \pm 5/2\rangle$ contributes to the magnetic moment. We can therefore estimate $g^{||}$ using the expression $\mu^{||}{}_{\text{eff}} = g^{||}{}_J\sqrt{J(J+1)}$ by taking $J = 1/2$ and the experimentally obtained value of 3.43 $\mu_B$/Ce for $\mu^{||}{}_{\text{eff}}$. This gives a value of $g^{||} \sim 4$, which agrees fairly nicely with the value reported previously using the electron spin-resonance (ESR) study [28]. The value of $\Theta_{cw}^{\parallel} = 0.017$ K obtained from the low-temperature fit still positive, but its value has now been reduced to <1 K.

Similar analysis for $\chi^{\perp}(T)$ yields $\chi_0^{\perp} \sim 2.7 \times 10^{-4}$ emu mol$^{-1}$ Oe$^{-1}$; $C^{\perp} = 0.75$ emu mol$^{-1}$ Oe$^{-1}$, giving $\mu_{\text{eff}}^{\perp} = 2.46$ $\mu_B$/Ce. The value of the effective moment is less than the theoretical value. The value of $\Theta_{cw}^{\perp}$ turned out to be −32.7 K. The negative sign of $\Theta_{cw}^{\perp}$ indicates the interaction between the Ce moments is antiferromagnetic in the *ab* plane. As above, the enhanced magnitude of $\Theta_{cw}^{\perp}$ is due to the crystal-field splitting. From a similar low-temperature fit (see Table III), we estimate $g^{\perp}$ to be $\sim 0.17$, in good agreement with the ESR value of 0.17.

In samples with large magnetic anisotropy, it is often more insightful to analyze the powder averaged data. The powder susceptibility, shown in Fig. 5, agrees well with the calculated values obtained using equation $\chi_{\text{avg}} = \frac{2}{3}\chi^{\perp} + \frac{1}{3}\chi^{\parallel}$. The Curie-Weiss analysis similar to the one above yielded the values of fitting parameters consistent with the single-crystal values, as shown in Table III. The negative sign of the Weiss temperature for the powder sample indicates that the average Ce-Ce interaction in $CeCl_3$ is antiferromagnetic in nature. The low-temperature fit gives a value of $\Theta_{cw} = -0.12$ K, which is negative and small as expected and is closer to the actual ordering temperature.

### 2. *Crystal-field analysis*

The degeneracy of lowest $J$ multiplet in an isolated $Ce^{3+}$ ion ($S = \frac{1}{2}$, $L = 3$ and J $= 5/2$) is $2J + 1 = 6$. In a trigonal crystalline electric field (CEF), this degeneracy is lifted by splitting the ground state into three Kramers doublets. The CEF Hamiltonian is given by

$$H_{\text{CEF}} = \sum_{m,n} B_m^n O_m^n, \tag{1}$$

where $B_m^n$ are the CEF parameters, and $O_m^n$ are the Stevens operators. Since the trigonal distortion in $CeCl_3$ is at best marginal, for the purpose of CEF analysis we can assume the point-group symmetry to be hexagonal. With this simplification, the only nonzero parameters in Eq. (1) are $B_2^0$ *and* $B_4^0$ [29,30]. Hence, we rewrite Eq. (1) as

$$H_{\text{CEF}} = B_2^0 O_2^0 + B_4^0 O_4^0. \tag{2}$$

Now, the magnetic susceptibility can be calculated using the van Vleck formula [31]:

$$\chi_i = \frac{2N_A g_j^2 \mu_B^2}{Z}\left[\sum_n \beta |\langle J_{i,n}\rangle|^2 e^{-\beta E_n} + 2\sum_{m \neq n} |\langle m|J_{i,n}|n\rangle|^2 \left(\frac{e^{-\beta E_m} - e^{-\beta E_n}}{E_n - E_m}\right)\right], \tag{3}$$

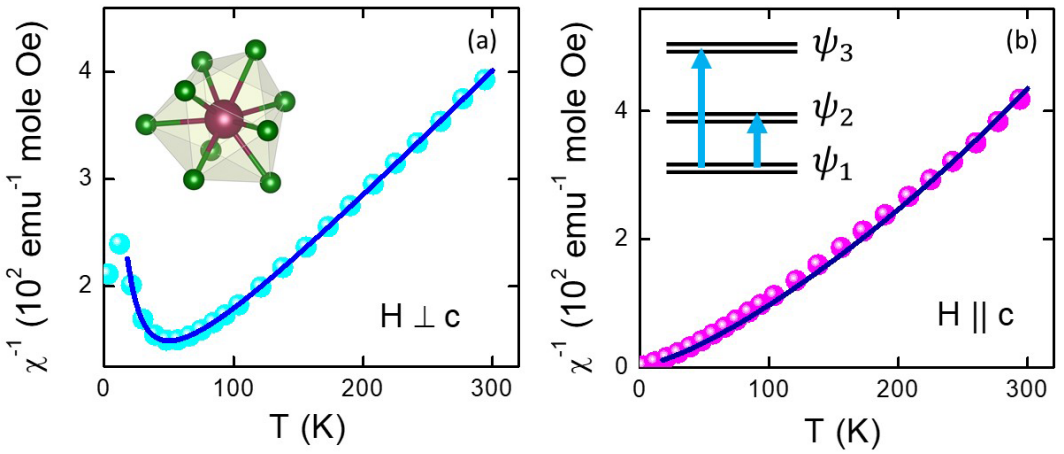


FIG. 6. $\chi^{-1}(T)$ plotted as a function of temperature for the orientations (a) $H \perp c$ (b) $H \parallel c$. The lines through the data points are best-fit curves obtained using the crystal electric-field analysis (see text for details). The inset in (a) shows the arrangement of ligand ions around the $Ce^{3+}$ ion at the center. The inset in (b) shows the crystal-field splitting of the lowest $J = 5/2$ multiplet of $Ce^{3+}$.

where, $N_A = 6.023 \times 10^{23}$ is the Avogadro number, $g_J = 6/7 \sim 0.857$, $\mu_B = 0.927 \times 10^{-20}$erg Oe$^{-1}$, $\beta = 1/k_BT$, $k_B = 1.38 \times 10^{-16}$ erg K$^{-1}$, $Z = \sum_n e^{-\beta E_n}$, and $n, m = 0,\ 1,\ 2$. Here, index $i$ corresponds to the orientation: $i = x$ for H$\perp c$, and $i = z$ for H $\parallel c$. As shown in Ref. [31], for the hexagonal symmetry, the eigenstates of Hamiltonian (2) are simply the unmixed or pure states of the form $|5/2,\ \pm 5/2\rangle$, $|5/2, \pm 3/2\rangle$, and $|5/2,\ \pm 1/2\rangle$. We know from the low-temperature magnetic susceptibility analysis that the crystal-field split ground state is $|5/2,\ \pm 5/2\rangle$, which implies that the first excited state is either $|5/2, \pm 3/2\rangle$ or $|5/2, \pm 1/2\rangle$. We tried both these combinations and found that only in the case where $|5/2, \pm 1/2\rangle$ is taken as the first excited state gives the satisfactory result. The expressions for $\chi^{\perp}$ and $\chi^{\parallel}$ using $|5/2, \pm 1/2\rangle$ as the first excited state and $|5/2, \pm 3/2\rangle$ as the highest state are as follows:

$$\chi^{\perp} = \frac{N_A g_j^2 \mu_B^2}{Z k_B}\left[\frac{9}{2}\frac{e^{-\beta E_1}}{T} + 5\left(\frac{1 - e^{-\beta E_2}}{E_2}\right) + 8\left(\frac{e^{-\beta E_2} - e^{-\beta E_1}}{E_1 - E_2}\right)\right], \quad (4)$$

$$\chi^{\parallel} = \frac{N_A g_j^2 \mu_B^2}{2 Z k_B}\left(\frac{25 + e^{-\beta E_1} + 9e^{-\beta E_2}}{T}\right), \quad (5)$$

where $Z = 2(1 + e^{-\beta E_1} + e^{-\beta E_2})$, and $E_1$ and $E_2$ are the energy eigenvalues measured with respect to the ground-state doublet. The inverse of expressions (4) and (5) are fitted to the experimental $\chi^{-1}(T)$. Figures 6(a) and 6(b) show the fitting result for $E_1 = 61\ K$ and $E_2 = 218\ K$. The CEF splitting scheme is shown in the inset of Fig 6(b), where $\Psi_1 = |5/2,\ \pm 5/2\rangle$, $\Psi_2 = |5/2, \pm 1/2\rangle$, and $\Psi_3 = |5/2,\ \pm 3/2\rangle$. These values are in good agreement with Schaack *et al.*, who predicted these splittings to be 47 cm$^{-1}$ ($\sim$ 68 K) and 116 cm$^{-1}$ ($\sim$ 167 K) using magneto-Raman spectroscopy [27].

### E. Isothermal magnetization

Isothermal magnetization, $M(H)$, plots at 2 K for both orientations ($H \perp c$ and $H \parallel c$) are shown in Fig. 7. A large anisotropy is observed between the two orientations. Along the perpendicular orientation, the magnetization is small and linear up to 160 kOe. On the other hand, when the field is applied parallel to the $c$ axis, $M(H)$ tends to saturate above a relatively small field of 20 kOe. A saturation magnetization value of $M_s = 2.17\ \mu_B$/f.u. is close to the saturation moment calculated theoretically, using, $M_s = J g_{||} \mu_B \approx 2\ \mu_B$ with $J = \frac{1}{2}$ and $g_{||} \approx 4$. The entire range of $M(H)$ data could be nicely fitted using the Brillouin function as shown in Fig. 7.

### F. Specific heat

The specific heats of $CeCl_3$ and $LaCl_3$, the latter being the nonmagnetic structural analog of $CeCl_3$, are measured between 250 and 2 K as shown in Fig. 8(a). The low-temperature data for $LaCl_3$ can be fitted using the expression $C_p = \gamma T + \beta T^3$,where $\gamma$ and $\beta$ correspond to electronic and lattice contributions, respectively. Since $LaCl_3$ is an insulator with an electronic band gap of 5.1 eV [13], the first electronic term can be ignored. The data are replotted as $C_p/T$ vs $T^2$ and the variation appears linear [inset in Fig. 8(a)]. Performing a linear-fit

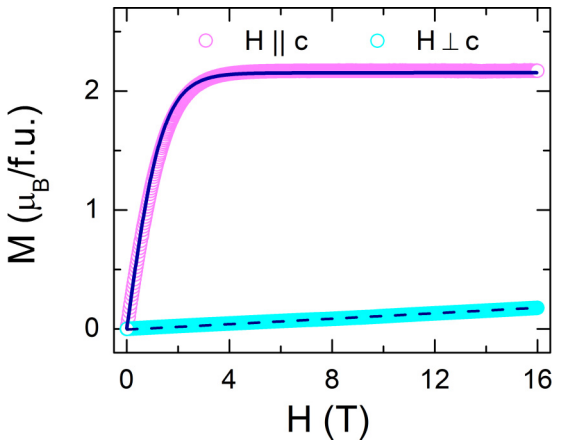


FIG. 7. The isothermal magnetization $M(H)$ at 2 K for the orientations $H \perp c$ and $H \parallel c$. The solid line is a fit to the data. The dashed line is a guide to the eye (see text for details).

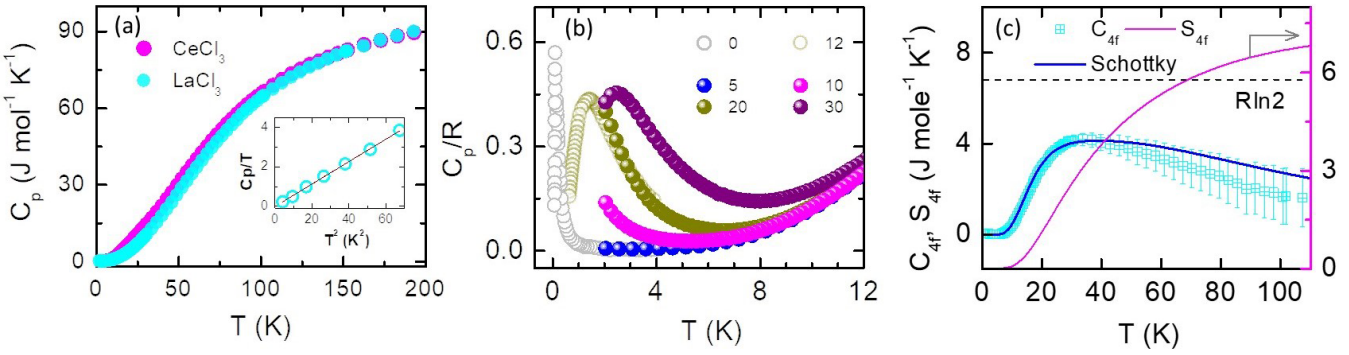


FIG. 8. (a) The specific heat ($C_p$) of $CeCl_3$ and its nonmagnetic analog $LaCl_3$ plotted as a function of temperature. Inset shows $C_p/T$ of $LaCl_3$ plotted against $T^2$. The line through the data points is a linear fit to extract the Debye temperature (see text for details). (b) $C_p/R$, where R is the gas constant, plotted as a function of temperature for applied magnetic fields of $H = 5$, 10, 20, and 30 kOe. Low-temperature zero-field and 12 kOe plots are recreated using data from Landau *et al.* [14], where $C_p$ is given in the range $T < 4.2$ K and $H < 14$ kOe. (c) $C_{4f}$ and $S_{4f}$ are plotted as a function of temperature. The solid line through the data points ($C_{4f}$) is a three-level Schottky fit using the crystal-field splitting estimated from the magnetic susceptibility data (see text for details).

yield: $\beta$ = slope = $5.68 \times 10^{-4}$ J mol$^{-1}$ K$^{-4}$. From this, we calculate the Debye temperature $\Theta_D = 239$ K using the formula $\beta = 12\pi^4 NR/5\Theta_D^3$ where $R$ is the universal gas constant. Note that this value of $\Theta_D$ is not the same as reported by Landau *et al.* ($\Theta_D = 155$ K) [14]. Upon examining their data closely, we found that the value of $\Theta_D$ obtained by them does not consider the factor $N$ (number of atoms per formula unit = 4), which explains the observed discrepancy. At high temperatures, the specific heat rises, towards the Dulong-Petit value of $3NR$ ($\approx 100$ J mol$^{-1}$ K$^{-1}$). In order to extract the $4f$ contribution to the specific heat, we subtracted the lattice part assuming nonmagnetic $LaCl_3$ as the lattice template for $CeCl_3$. Being isostructural to $CeCl_3$ and having a comparable molecular weight, $LaCl_3$ is a closest match to model the lattice specific heat of $CeCl_3$. Figure 8(c) shows the $4f$ electrons contribution ($C_{4f}$) in zero field above 2 K. The $C_{4f}$ rises sharply above 2 K, showcasing a broad peak centered around 30 K. This is attributed to the Schottky anomaly associated with the higher lying crystal field split Kramers doublets. $C_{4f}$ is therefore fitted using the three-level Schottky expression, given by Eq. (6) below:

$$C_{\text{Schottky}} = R\frac{1}{T^2}\left\{\frac{\left(g_1 g_0 E_1^2 e^{-\beta E_1} + g_2 g_0 E_2^2 e^{-\beta E_2}\right)}{\left(g_0 + g_1 e^{-\beta E_1} + g_2 e^{-\beta E_2}\right)^2} + \frac{\left(g_1 g_2 e^{-\beta(E_1+E_2)}\right)[E_1(E_1-E_2)+E_2(E_2-E_1)]}{\left(g_0 + g_1 e^{-\beta E_1} + g_2 e^{-\beta E_2}\right)^2}\right\}, \quad (6)$$

where $E_1$ and $E_2$ are the energies of the first and second excited doublets above the ground state, $g_0 = g_1 = g_2 = 2$ is the degeneracy of the states [32]. The best fit to the experimental data is obtained for $E_1 = 67$ K and $E_2 = 200$ K. While the position of the first excited state is in good agreement with previous report, the energy of the higher-lying excited state is somewhat higher than the value of 167 K reported using magneto-Raman spectroscopy [14,27]; however, the agreement with the values obtained using the susceptibility analysis is satisfactory.

We come now to the field dependence of low-temperature specific heat of our $CeCl_3$ crystal. The magnetic-field dependent measurements are summarized in Fig. 8(b). The in-field measurements ($H \parallel a$) are superimposed with the data from the previous study [14], where specific heat is reported only below 4.2 K and up to a maximum applied magnetic field of 12 kOe. Our zero-field data overlap nicely with the zero-field data in Ref. [14]. In zero-field, $C_p$ shows an upturn below 1 K, which is a precursory rise leading to the long-range ordering of the Ce moments at $T_N \sim 0.11$ K [14]. The magnetic entropy below 2 K ($\approx R\ln 2$) corroborates the long-range ordering (*vide infra*). Due to a weak exchange coupling between the Ce moments, even a small applied magnetic field has a relatively strong effect on the specific heat peak, which broadens and shifts toward higher temperatures as the field strength increases, occurring near 2.5 K in an applied magnetic field of 30 kOe. Unfortunately, our attempts to measure the specific heat at higher field turned unsuccessful as the crystal got dislodged from the sample platform and shattered into pieces upon cooling below 4.5 K under a field of 50 kOe. This is due to the strong magnetic torque that acts on the specimen due to huge anisotropy and large, but weakly interacting, magnetic moments. A slight discrepancy between the infield data in our study and those taken from Ref. [14] (12 kOe data from Ref. [14] is close to our 20 kOe), may arise from the actual value of the applied field and the crystal orientation.

We estimated the entropy associated with the $4f$ electrons, $S_{4f}$, above $T_0 = 2$ K, using the formula: $S_{4f} = \int_{T_0}^{T_1} C_{4f}/T' dT'$. As shown in Fig. 8(c), the recovered entropy exceeds the $R\ln 2$ value near 70 K and continues to rise up to the highest temperature in our measurements. This behavior needs a comment: first, we have not considered a large chunk of $S_{4f}$ buried below 2 K, the range over which the Ce moments order magnetically. If we do this by including the low-temperature specific-heat data from previous literature [14], the resulting $S_{4f}$ plot plateau at $R\ln 2$ around 2 K, and this plateau stretches

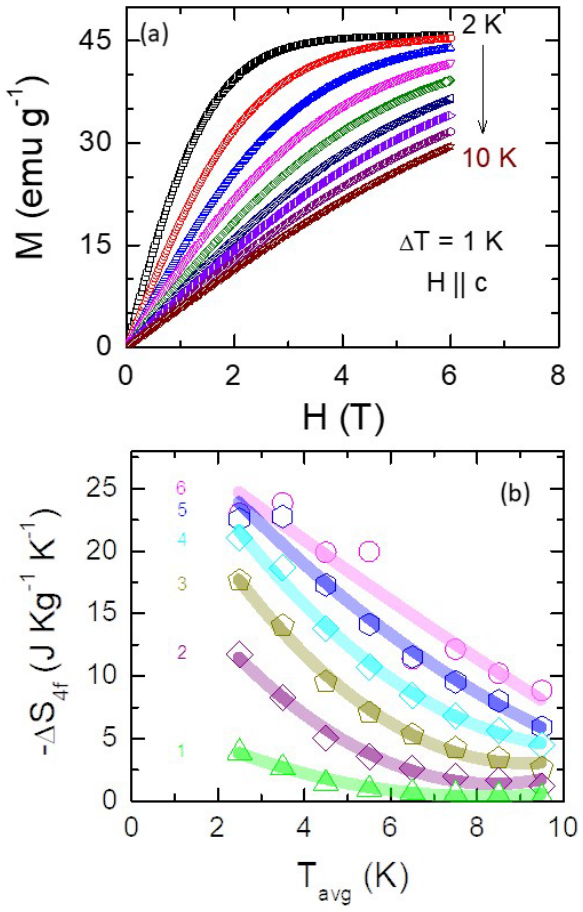


FIG. 9. (a) Isothermal magnetization from $T = 2$ to 10 K at $\Delta T = 1$ K interval. The field is applied parallel to the easy axis (0 0 1) of magnetization. (b) The change in entropy as a measure of the magnetocaloric effect is plotted as a function of $T_{\text{avg}}$ (see text for details).

up to 10 K. Thus, the first excited state starts contributing to $S_{4f}$ any substantially only around 10 K, the temperature above which $C_{4f}$ in Fig. 8(c) rises sharply. As shown in the Supplemental Material [23], Fig. S6, the total $S_{4f}$ (i.e., including the low-temperature contribution) overshoots the value $R\ln 4$ near 70 K. Thus, $S_{4f}$ crossing $R\ln 2$ near 70 K in Fig. 8(c) is the contribution sans the $R\ln 2$ contribution from the ground-state doublet.

### G. Magnetocaloric effect

A weak exchange coupling between the Ce-moments, a large magnetic moment in the crystal field split ground state, and a strong magnetic anisotropy are good indicators that $CeCl_3$ may show a high magnetocaloric effect. In order to estimate the magnetocaloric effect, magnetization isotherms are plotted at different temperatures to obtain the change in the magnetic entropy. The measurements were done with the field applied along the crystallographic $c$-axis. Figure 9(a) shows the $M(H)$ isotherms from 2 K to 10 K with a temperature interval $\Delta T = 1$ K. For $\Delta H = 6$ T, the change in magnetic entropy is plotted as a function of average temperature, as shown in Fig. 9(b). The maximum entropy change $-\Delta S_m = 23 \pm 1$ J Kg$^{-1}$ K$^{-1}$ is observed near 2.5 K for $\Delta H = 50$–60 kOe. This is a reasonably high value, making $CeCl_3$ a potential magnetocaloric material to be used as a cryogenic magnetic coolant. However, the highly hygroscopic nature of this material must also be taken into consideration, which may require the coolant material to be permanently sealed in a nonmagnetic but highly electrically conducting capsule. In Table IV below, we list $-\Delta S_m$ for a range of magnetocaloric materials that undergo long-range magnetic ordering below 2 K. Among the known Ce-based compounds where magnetocaloric effect has been evaluated, $CeCl_3$ perhaps showcases the highest $-\Delta S_m$, which is in many cases is comparable to the Gd-based compounds. This is not surprising given the high $J$ value in the crystal field split ground state of $CeCl_3$. Taking into consideration that the ordering temperature of $CeCl_3$ is an order of magnitude below our measurement temperature range, a higher $-\Delta S_m$ value at an even lower field is expected if the measurements are extended to lower temperatures.

## IV. SUMMARY AND CONCLUSIONS

High-quality single crystals of $CeCl_3$ are grown using modified Bridgman and Bridgman-Stockbarger methods. Using both methods, millimeter-sized single crystals are could be grown. The crystals obtained using the Bridgman-Stockbarger method are larger in size, fully transparent, and higher in yield compared to the crystals obtained using the static Bridgman technique. The grown crystals are highly sensitive to moisture and decompose within few minutes when exposed to ambient air to form a white powder (hexahydrate). While the overall crystal structure of $CeCl_3$ is hexagonal, the single-crystal x-ray diffraction show very weak (0 0 $l$) superstructure reflections indicating a slight trigonal distortion. The low-temperature thermal and magnetic properties of the grown crystals are studied between 2 and 300 K. The magnetic susceptibility is measured as a function of temperature for two different orientations, namely, $H \parallel c$ and $H \perp c$, in addition to the measurements done on polycrystalline sample. In $H \perp c$ data, a broad and prominent susceptibility peak, centered around 50 K, is observed. The susceptibility for the $H \parallel c$, on the other hand, is not only two orders of magnitude larger but also shows a monotonic Curie-like increase upon cooling. We analyzed the susceptibilities along the two orientations using the crystal-field theory. Due to crystal field the ground-state $J$ manifold ($J = 5/2$) of $Ce^{3+}$ shown to split into three Kramers doublets. The eigenstates and energies of these doublets are found to be $\psi_1 = |5/2, \pm 5/2\rangle$ (the ground state), $\psi_2 = |5/2, \pm 1/2\rangle$ (the first excited state at $E_1 \approx 61$ K), and $\psi_3 = |5/2, \pm 3/2\rangle$ (the second excited doublet at $E_2 \approx 218$ K). Using these parameters, the susceptibility behavior along the two orientations is successfully described. In the crystal field split ground state of $Ce^{3+}$, the large Ce moment is constrained to point along the $c$-axis, acting like an Ising system. This is manifested in the isothermal magnetization measured along the two orientations. The $M(H)$ curve is linear and the $M(H)$ values are very small for $H \perp c$, whereas $M(H)$ saturates readily above $\sim 30$ kOe in the $H \parallel$ c orientation, depicting that $c$ axis is the easy axis of magnetization.

TABLE IV. A comparison of $-\Delta S_m$ (maximum change in the magnetic entropy) for various previously studied potential cryogenic magnetic coolants at $T_{\min}$ (lowest temperature of measurement) and $H_{\max}$ (maximum applied magnetic fields).

| Class of material | Compound | $\Delta S_{\max}$ (J Kg$^{-1}$ K$^{-1}$) | $T_N/T_C$ (K) | $T_{\min}$ (K) | $H_{\max}$ (kOe) | Ref. |
|---|---|---|---|---|---|---|
| $RCl_3$ | $CeCl_3$ | 23.0 | 0.11 | 2.5 | 60 | This work |
| Garnets $R_3Ga_5O_{12}$ | $Gd_3Ga_5O_{12}$ | 35.3 | $< 0.025$ | 2 | 60 | [33] |
| | $Dy_3Ga_5O_{12}$ | 14.5 | 0.37 | 2 | 60 | [33] |
| | $Tb_3Ga_5O_{12}$ | 11.2 | 0.25 | 4 | 40 | [33] |
| | $Nd_3Ga_5O_{12}$ | 16 | 0.52 | 1 | 50 | [33] |
| $R(OH)_3$ | $Er(OH)_3$ | 26.5 | $< 2$ | 4 | 50 | [34] |
| $RF_3$ | $GdF_3$ | 67.1 | $< 2$ | 2 | 50 | [35] |
| | $Cd_{0.9}Gd_{0.1}F_{2.1}$ | 7.2 | $< 2$ | 5 | 50 | [36] |
| | $Cd_{0.9}Tb_{0.1}F_{2.1}$ | 2.7 | | 5 | 50 | [36] |
| | $Cd_{0.9}Dy_{0.1}F_{2.1}$ | 0.8 | | 5 | 50 | [36] |
| Pyrochlores | $Gd_2Sn_2O_7$ | 32 | 1 | 2 | 90 | [37] |
| | $Gd_2Ti_2O_7$ | 17.9 | $< 2$ | 2.5 | 50 | [38] |
| Tripod kagome | $Gd_3Mg_2Sb_3O_{14}$ | 33 | 1.7 | 2 | 90 | [37] |
| Double perovskite | $Ba_2GdSbO_6$ | 24 | $< 0.4$ | 2 | 70 | [39] |

The specific heat is measured in the temperature range from 2 to 300 K. No anomalies could be seen at any temperature within the measurement range except for a weak upturn at low temperatures, which is attributed to the short-range correlations between the Ce moments. The analysis of $4f$-derived magnetic specific heat, showcasing a Schottky anomaly, is successfully done using the crystal-field scheme obtained from the magnetic susceptibility analysis. The low-temperature magnetic field undergoes spectacular changes in the presence of a magnetic field. With increasing applied magnetic field, the low-temperature upturn becomes more pronounced and shifts to higher temperatures, showcasing a peak above 2 K in fields as small as 25 kOe.

The weak exchange coupling between the Ce moments, a strong Ising-like anisotropy, and a large magnetic moment are ideal settings for realizing a high magnetocaloric effect. Indeed, we found a maximum entropy change of $-\Delta S_m = 23 \pm 1$ J Kg$^{-1}$ K$^{-1}$ at 2.5 K in the field range 50–60 kOe. This value of $-\Delta S_m$ lies in the same ballpark as the best results in previous literature on some Gd-based compounds. This makes $CeCl_3$ a potential magnetocaloric material for cryogenic applications as a magnetic coolant. The Raman spectrum of $CeCl_3$ exhibits five Raman-active modes at 106.8, 181.2, 189, 213, and 219.7 cm$^{-1}$. In the future, polarization, temperature, and magnetic-field dependent Raman spectroscopy are needed to completely understand the evolution of Raman modes and the correlation between the spin and lattice degrees of freedom. The degenerate infrared active $E_{1u}$ phonon mode will be interesting to study in future as the electric dipole moment associated with this phonon can be resonantly excited by the electric field of the applied laser pulse. This can yield large vibrational amplitudes that can act on the spins through the inverse spin-phonon coupling as predicted in a recent theoretical work [17]. Since the *nn* and *nnn* exchange interactions are of comparable magnitude, further investigations using neutron scattering and muon spin-relaxation techniques would be useful in capturing the exact magnetic ground state and excitations of $CeCl_3$.

## ACKNOWLEDGMENTS

The authors thank Dr. Sitaram Ramakrishnan for fruitful discussion on single crystal structure refinement. S.S. thanks financial assistance received under the Scheme for Transformational and Advanced Research in Sciences (STARS) by the Ministry of Education, Government of India (sanction order no. STARS/APR2019/PS/358/FS). S.S. and L.H. thank I-HUB Quantum Technology Foundation (I-HUB QTF), National Mission on Interdisciplinary Cyber Physical Systems (NM-ICPS), hosted by Indian Institute of Science Education and Research, Pune for financial assistance. N.P. would like to thank Council for Scientific and Industrial Research (CSIR) for Ph.D. fellowship.

[1] L. Balents, Spin liquids in frustrated magnets, Nature (London) **464**, 199 (2010).

[2] A. Kitaev, Anyons in an exactly solved model and beyond, Ann. Phys. (N. Y.). **321**, 2 (2006).

[3] G. Jackeli and G. Khaliullin, Mott insulators in the strong spin-orbit coupling limit: From heisenberg to a quantum compass and kitaev models, Phys. Rev. Lett. **102**, 017205 (2009).

[4] J. Chaloupka and G. Khaliullin, Magnetic anisotropy in the kitaev model systems $Na_2IrO_3$ and $RuCl_3$, Phys. Rev. B **94**, 064435 (2016).

[5] S. Widmann, V. Tsurkan, D. A. Prishchenko, V. G. Mazurenko, A. A. Tsirlin, and A. Loidl, Thermodynamic evidence of fractionalized excitations in $\alpha-RuCL_3$, Phys. Rev. B **99**, 094415 (2019).

[6] J. A. N. Bruin, R. R. Claus, Y. Matsumoto, N. Kurita, H. Tanaka, and H. Takagi, Robustness of the thermal hall effect close to half-quantization in $\alpha$-$RuCl_3$, Nat. Phys. **18**, 401 (2022).

[7] J. Xing *et al.*, Néel-type antiferromagnetic order and magnetic field-temperature phase diagram in the spin-12 rare-earth honeycomb compound $YbCl_3$, Phys. Rev. B **102**, 014427 (2020).

[8] G. Sala *et al.*, Crystal field splitting, local anisotropy, and low-energy excitations in the quantum magnet $YbCl_3$, Phys. Rev. B **100**, 180406(R) (2019).

[9] Y. Hao *et al.*, Field-tuned magnetic structure and phase diagram of the honeycomb magnet $YbCl_3$, Sci. China Phys., Mech. Astron. **64**, 237411 (2020).

[10] W. H. Zachariasen, Crystal chemical studies of the 5f-series of elements. I. New structure types, Acta Crystallogr. **1**, 265 (1948).

[11] B. Morosin, Crystal structures of anhydrous rare-earth chlorides, J. Chem. Phys. **49**, 3007 (1968).

[12] D. H. Templeton and C. H. Dauben, Lattice parameters of some rare earth compounds and a set of crystal radii, J. Am. Chem. Soc. **76**, 5237 (1954).

[13] K.-H. Park and S.-J. Oh, Electron-spectroscopy study of rare-earth trihalides, Phys. Rev. B **48**, 14833 (1993).

[14] D. P. Landau, J. C. Doran, and B. E. Keen, Thermal and magnetic properties of $CeCl_3$, Phys. Rev. B **7**, 4961 (1973).

[15] J. H. Colwell, B. W. Mangum, and D. B. Utton, Low-temperature magnetic properties of some hexagonal rare-earth trihalides, Phys. Rev. **181**, 842 (1969).

[16] D. P. Landau, R. J. Birgeneau, M. T. Hutchings, and W. P. Wolf, Interaction constants in $CeCl_3$, J. Appl. Phys. **39**, 975 (1968).

[17] D. M. Juraschek, T. Neuman, and P. Narang, Giant effective magnetic fields from optically driven chiral phonons in 4f paramagnets, Phys. Rev. Res. **4**, 013129 (2022).

[18] J. Luo, T. Lin, J. Zhang, X. Chen, E. R. Blackert, R. Xu, B. I. Yakobson, and H. Zhu, Large effective magnetic fields from chiral phonons in rare-earth halides, Science **382**, 698 (2023).

[19] J. H. Freeman and M. L. Smith, The preparation of anhydrous inorganic chlorides by dehydration with thionyl chloride, J. Inorg. Nucl. Chem. **7**, 224 (1958).

[20] H. Gunsilius, W. Urland, and R. Kremer, Darstellung von Selten-Erd-Trichloriden über chemischen transport mit aluminiumtrichlorid, Z. Anorg. Allg. Chem. **550**, 35 (1987).

[21] S. Mroczkowski, Preparation of single crystals of $EuCl_3$ and related polyvalent halides, J. Cryst. Growth **6**, 147 (1970).

[22] N. Pistawala, D. Rout, K. Saurabh, R. Bag, K. Karmakar, L. Harnagea, and S. Singh, Crystal growth of quantum materials: A review of selective materials and techniques, Bull. Mater. Sci. **45**, 10 (2021).

[23] See Supplemental Material at http://link.aps.org/supplemental/10.1103/PhysRevMaterials.8.076201 for x-ray diffraction (powder and single crystal), Raman, structural refinement parameters, and magnetic heat capacity.

[24] K. Momma and F. Izumi, VESTA 3 for three-dimensional visualization of crystal, volumetric and morphology data, J. Appl. Crystallogr. **44**, 1272 (2011).

[25] T. C. Damen, A. Kiel, S. P. S. Porto, and S. Singh, The raman effects of $CeCl_3$ and $PrCl_3$, Solid State Commun. **6**, 671 (1968).

[26] J. T. Hougen and S. Singh, Electronic and vibrational Raman spectra of $PrCl_3$ and $LaCl_3$, Proc. R. Soc. Lond. A **277**, 193 (1964).

[27] G. Schaack, Magnetic field dependent splitting of doubly degenerate phonon states in anhydrous cerium-trichloride, Z. Phys. B **26**, 49 (1977).

[28] C. A. Hutchison and E. Wong, Paramagnetic resonance in rare earth trichlorides, J. Chem. Phys. **29**, 754 (1958).

[29] M. T. Hutchings, *Point-Charge Calculations of Energy Levels of Magnetic Ions in Crystalline Electric Fields*, edited by F. Seitz and D. Turnbull, Solid State Physics Vol. 16 (Academic Press, New Haven, Connecticut, 1964), pp. 227–273.

[30] K. W. H. Stevens, Matrix elements and operator equivalents connected with the magnetic properties of rare earth ions, Proc. Phys. Soc. Sect. A **65**, 209 (1952).

[31] J. Banda, B. K. Rai, H. Rosner, E. Morosan, C. Geibel, and M. Brando, Crystalline electric field of Ce in trigonal symmetry: $CeIr_3Ge_7$ as a model case, Phys. Rev. B **98**, 195120 (2018).

[32] M. de Souza, R. Paupitz, A. Seridonio, and R. E. Lagos, Specific heat anomalies in solids described by a multilevel model, Braz. J. Phys. **46**, 206 (2016).

[33] M. Kleinhans, K. Eibensteiner, J. C. Leiner, C. Resch, L. Worch, M. A. Wilde, J. Spallek, A. Regnat, and C. Pfleiderer, Magnetocaloric properties of $R_3Ga_5O_{12}$ ($R$ = Tb, Gd, Nd, Dy), Phys. Rev. Appl. **19**, 014038 (2023).

[34] P. W. Doheny, J. Chen, T. Gruner, F. M. Grosche, and P. J. Saines, $Dy(OH)_3$: A paramagnetic magnetocaloric material for hydrogen liquefaction, J. Mater. Chem. A **11**, 26474 (2023).

[35] Y.-C. Chen, J. Prokleška, W.-J. Xu, J.-L. Liu, J. Liu, W.-X. Zhang, J.-H. Jia, V. Sechovský, and M.-L. Tong, A brilliant cryogenic magnetic coolant: Magnetic and magnetocaloric study of ferromagnetically coupled $GdF_3$, J. Mater. Chem. C **3**, 12206 (2015).

[36] A. Fernández, X. Bohigas, J. Tejada, E. A. Sulyanova, I. I. Buchinskaya, and B. P. Sobolev, The magnetocaloric effect in high-spin paramagnetic rare-earth fluorites, Mater. Chem. Phys. **105**, 62 (2007).

[37] E. C. Koskelo, P. Mukherjee, C. Liu, A. C. Sackville Hamilton, H. S. Ong, C. Castelnovo, M. E. Zhitomirsky, and S. E. Dutton, Comparative study of magnetocaloric properties for $Gd^{3+}$ compounds with different frustrated lattice geometries, PRX Energy **2**, 033005 (2023).

[38] B. Xu, H. Xie, Z. Mo, X. Gao, J. Wang, Z. Li, and J. Shen, Magnetic properties and cryogenic magnetocaloric effect of pyrochlore structure $RE_2Ti_2O_7$ (RE = Gd, Tb, and Ho) compounds, J. Appl. Phys. **135**, 75104 (2024).

[39] E. C. Koskelo, N. D. Kelly, L. A. V. Nagle-Cocco, J. D. Bocarsly, P. Mukherjee, C. Liu, Q. Zhang, and S. E. Dutton, Magnetic and magnetocaloric properties of the $A_2LnSbO_6$ lanthanide oxides on the frustrated fcc lattice, Inorg. Chem. **62**, 10317 (2023).